Understanding the High Strength and Good Ductility in LPSO-Containing Mg Alloy Using Synchrotron X-ray Diffraction

JIE WANG, LEYUN WANG, GAOMING ZHU, BIJIN ZHOU, TAO YING, XINGMIN ZHANG, QI HUANG, YAO SHEN, XIAOQIN ZENG, and HAIYAN JIANG

Mg alloys containing long-period stacking-ordered (LPSO) phases often display excellent mechanical properties. The underlying mechanism is yet unclear. In this work, *in situ* synchrotron X-ray diffraction was employed to study tensile deformation of a $Mg_{97}Y_2Zn$ alloy that contains 18R-type LPSO phase. From lattice strain measurement, it is found that the LPSO phase has a similar elastic modulus as Mg. After material yielding, lattice strain in the Mg phase decreased, while lattice strain in the LPSO phase increased further. By analyzing the lattice strain evolution of different Mg peaks, basal slip and deformation twinning are identified as the dominant deformation mechanisms. This finding is further confirmed by surface slip trace analysis using electron backscattered diffraction (EBSD). Additional analysis of diffraction peak broadening indicates a continuous increase of dislocation density during plastic deformation. Based on the above results, it can be concluded that the interdendritic LPSO phase behaves like a reinforcing phase that directly strengthens the material. The high tensile ductility of the material is attributed to the weak extrusion texture caused by the presence of interdendritic LPSO. In addition, small LPSO plates inside the Mg phase can serve as dislocation nucleation sites, which leads to a high work hardening rate in the material.

I. INTRODUCTION

MG alloys have gained increasing attention as candidate material for structural applications due to their high specific strength. On the other hand, the low absolute strength and poor ductility at room temperature remain a bottleneck for the widespread use of Mg.[1] Mg-Y-Zn alloys that contain a long-period stacking-ordered (LPSO) structure have been found to possess both high strength and good ductility compared with many other Mg alloys.[2–4] The LPSO structure is both chemically and structurally ordered, with Y and Zn atoms occupying specific sites in the Mg lattice.[5,6]

To understand the excellent mechanical properties, deformation of LPSO-containing Mg alloys has been investigated in recent years. Shao *et al.*[7] studied the deformation microstructure of a $Mg_{97}Y_2Zn_1$ (at. pct) alloy after hot compression. They proposed that the interface between Mg and LPSO phases provides resistance against catastrophic fracture of the material. Hagihara *et al.*[8] examined the deformation microstructure of a directionally solidified $Mg_{88}Zn_5Y_7$ alloy after compression at room temperature. They found that basal slip was the dominant deformation mode in the LPSO phase. Kinking was also observed as a complementary deformation mechanism to accommodate local deformation in LPSO. In a recent work, Kim *et al.*[9] observed both basal $\langle a \rangle$ dislocations and pyramidal $\langle c+a \rangle$ dislocations in the Mg phase in a cold-rolled $Mg_{97}Y_2Zn_1$ alloy. Non-basal $\langle a \rangle$ slip was also observed in the LPSO phase in an extruded $Mg_{97}Y_2Zn_1$ alloy after tensile deformation.[10]

So far, most studies on the deformation of LPSO-containing Mg alloys were conducted using post-deformation samples by electron microscopy.[4–18] To fully understand the excellent combination of strength and ductility in this type of material, *in situ* tests are more

JIE WANG, LEYUN WANG, GAOMING ZHU, BIJIN ZHOU, TAO YING, and HAIYAN JIANG are with the National Engineering Research Center of Light Alloy Net Forming, Shanghai Jiao Tong University, Shanghai 200240, China. Contact e-mail: leyunwang@sjtu.edu.cn XINGMIN ZHANG is with the Shanghai Institute of Applied Physics, Chinese Academy of Sciences, Shanghai 201204, China. QI HUANG and YAO SHEN are with the State Key Laboratory of Metal Matrix Composites, Shanghai Jiao Tong University, Shanghai 200240, China. XIAOQIN ZENG is with the National Engineering Research Center of Light Alloy Net Forming, Shanghai Jiao Tong University and also with the State Key Laboratory of Metal Matrix Composites, Shanghai Jiao Tong University. Contact e-mail: xqzeng@sjtu.edu.cn

desirable. Synchrotron X-ray, due to its ability to penetrate bulk materials non-destructively, is a powerful tool for *in situ* studies of material deformation.[19,20] Among numerous synchrotron X-ray characterization techniques, X-ray diffraction (XRD) is particularly useful for understanding the structure–property relationship in engineering materials *via* various *in situ* experiments. It allows for quantitative assessment of load partitioning between different phases,[21–26] texture change,[27–29] and dislocation structure evolution[30–33] during deformation. Garces *et al.*[26] recently studied the compression behavior of an extruded $Mg_{97}Y_2Zn_1$ (at. pct) alloy and observed load transfer from the Mg phase to the LPSO phase based on lattice strain analysis. That study, however, did not fully address the question why these alloys possess good tensile ductility as well.

In the present work, we use *in situ* synchrotron X-ray diffraction to examine the tensile behavior of an extruded $Mg_{97}Y_2Zn_1$ (at. pct) alloy. By tracking lattice strain, diffraction intensity, and broadening of different diffraction peaks during the tensile test, deformation behaviors of both Mg and LPSO were analyzed. Based on these information, the origin of the high strength and good ductility in LPSO-containing Mg alloys is elucidated.

II. EXPERIMENTAL

A. *Material*

The $Mg_{97}Y_2Zn_1$ alloy was fabricated by melting pure Mg, pure Zn, and Mg-25 wt pct Y master alloy in an electric resistance furnace under a protective atmosphere of CO_2 (99 vol pct) and SF_6 (1 vol pct) gas mixture. The melt was held at 1023 K (750 °C) for ~30 minutes to ensure a homogeneous composition. Afterwards, the melt was casted into a preheated cylindrical steel mold. Chemical composition of the cast billet was found to be Mg-5.1Y-2.4Zn (wt pct) using Inductively Coupled Plasma Atomic Emission Spectroscopy (ICP-AES). The cast billet was homogenized at 673 K (400 °C) for 24 hours. Hot extrusion was then carried out at 623 K (350 °C) with the extrusion speed of 2 mm/s to produce round bars with a diameter of 14 mm, which amounts to an extrusion ratio of 18:1.

Optical micrographs (OM) of the as-cast and as-extruded materials were examined using Zeiss Axio Observer A1. Samples for OM examinations were polished and etched in a solution of 4 vol pct nitric acid + 96 vol pct ethanol for 10–15 seconds. Microstructure and texture of the as-extruded material were further characterized by scanning electron microscope (SEM, NOVA NanoSEM 230, FEI) and electron backscattered diffraction (EBSD, Oxford Instrument, UK). Samples for SEM and EBSD characterization were electrolytic polished in a solution of 10 vol pct perchloric acid + 90 vol pct ethanol at 30 V and 0.6 A under 253 K (− 20 °C) for 2.5 minutes. EBSD scans were conducted at an accelerating voltage of 20 kV with a scan step size of 0.8 μm. EBSD data were analyzed using the TSL OIM Analysis 7 software (EDAX Inc).

To explore the deformation mechanisms, a rectangular sample of 30 mm × 7.0 mm × 1.5 mm dimension was extracted from the as-extruded material, with the longitudinal axis being parallel to the extrusion direction. The sample was deformed by four-point bending to achieve an equivalent tensile strain of ~1.5 pct and then ~3.0 pct on the top surface. EBSD-based slip trace analysis was utilized to analyze the activated slip systems in different grains. A set of parallel slip lines observed in a given grain is caused by collective dislocation glide on a particular slip plane. Those slip lines should be parallel to the line of intersection of the slip plane and the sample surface plane. With the grain orientations measured by EBSD, we can calculate the theoretical slip line directions for all possible slip systems and compare them with the actually observed slip line to infer the activated slip system. Details of this method can be found in Reference 34.

B. *In Situ Synchrotron X-ray Diffraction*

For the *in situ* synchrotron X-ray diffraction experiment, subsize flat dog-bone tensile specimens were prepared by electrical discharge machining (EDM) with the tensile axis being parallel to the extrusion direction. The nominal gauge dimension of the specimen was 17 mm (L) × 1.5 mm (H) × 1.0 mm (T), as demonstrated in Figure 1. The *in situ* synchrotron X-ray diffraction experiment was conducted at Beamline BL14B1 of the Shanghai Synchrotron Radiation Facility (SSRF) in China. The beamline provides a medium energy (18 keV, λ = 0.688 Å) X-ray beam (200 μm × 200 μm). Given the low density of Mg, transmission of the X-ray through a 1-mm-thick specimen is approximately 55 pct (calculated at https://physics.nist.gov/PhysRefData/FFast/html/form.html). This level of transmission provides strong diffraction signals to be recorded by an area detector (3072 × 3072 pixels) on the other side. More details of the beamline can be found in Reference 35.

The specimen was deformed under tension by a micro-testing module (MTI, SEMtester 1000lb) at a constant crosshead speed of 0.2 mm/min, which amounts to a nominal strain rate of 2.0×10^{-4} s^{-1}. A diffraction pattern was recorded every 10 seconds while the specimen was being continuously deformed. From the timeline of the test, each diffraction pattern can be correlated with a strain value, which is the basis for *in situ* examination of microstructure evolution during deformation. The specimen-to-detector distance was approximately 299.4 mm according to the calibration using standard LaB_6 powders. The schematic setup of the *in situ* experiment is shown in Figure 1.

Peak rings in a diffraction pattern correspond to different crystallographic planes. Radial shift of peak rings during deformation provides information on the lattice strain of different (hkl) planes:

$$\varepsilon_{hkl}^i = \frac{d_{hkl}^i(\sigma) - d_{hkl}^i(0)}{d_{hkl}^i(0)}, \qquad [1]$$

where $d_{hkl}^i(0)$ $d_{hkl}^i(\sigma)$ are the *d*-spacing of the (hkl) plane in phase *i* before deformation and under applied stress
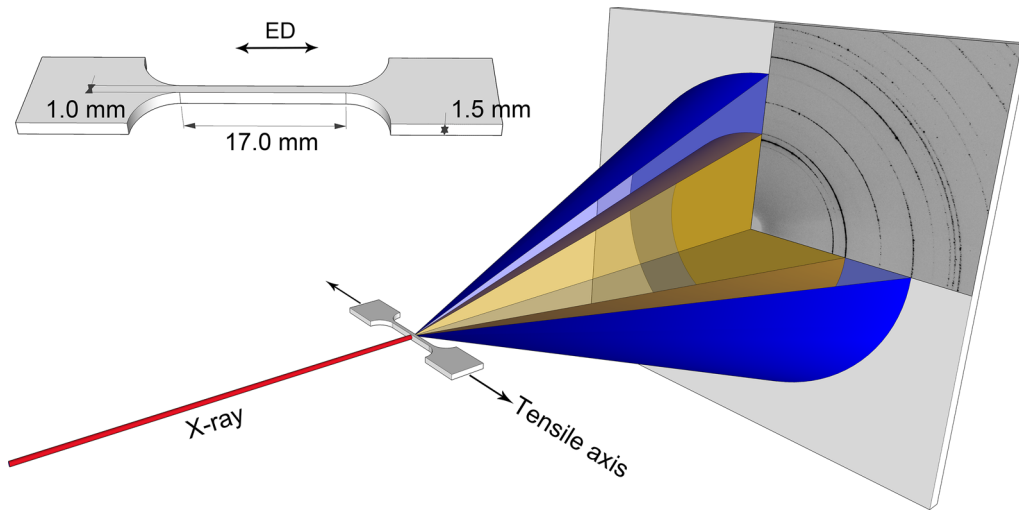
Fig. 1— Dimension of the tensile specimen and a schematic of the *in situ* tensile test with synchrotron X-ray diffraction.

σ. In addition to radial shifting, material deformation also causes broadening of peak rings, which is quantified by the full width at half-maximum (FWHM) value. In general, peak broadening has two parts: instrument broadening and sample broadening. The instrument broadening ($FWHM_{instrument}$) was calibrated using a standard LaB_6 powder sample and then subtracted from the total peak broadening ($FWHM_{total}$) to obtain the sample broadening part ($FWHM_{sample}$) as $FWHM^2_{sample} = FWHM^2_{total} - FWHM^2_{instrument}$. For the peak width analysis presented in this paper, the $FWHM_{sample}$ value is used.

III. RESULTS

A. *Microstructure of the Material*

Figure 2 shows optical micrographs of the $Mg_{97}Y_2Zn_1$ alloy at the as-cast and as-extruded conditions. The primary α-Mg phase in the as-cast material shows dendrite morphology while the LPSO phase is located in the interdendritic regions. According to the literature, the interdendritic LPSO phase in the as-cast material belongs to the 18R type.[9,36] After hot extrusion, the Mg phase exhibits a dynamically recrystallized (DRX) grain structure with the average grain size of ~10 μm. The interdendritic LPSO phase now turned into fibers along the extrusion direction. Volume fraction of the interdendritic LPSO is approximately 19.3 pct.

Microstructure of the as-extruded material was further characterized by EBSD. Figure 3(a) shows an EBSD phase map from a selected region in which the red color represents Mg phase and the blue color represents LPSO phase. The LPSO phase was indexed as the 18R type using the atomic coordinates given in Reference 4. Some regions of the LPSO phase could not be indexed and appear black in Figure 3(a). Inverse pole figure (IPF) maps with respect to the extrusion direction (ED) for LPSO phase and Mg phase are shown in
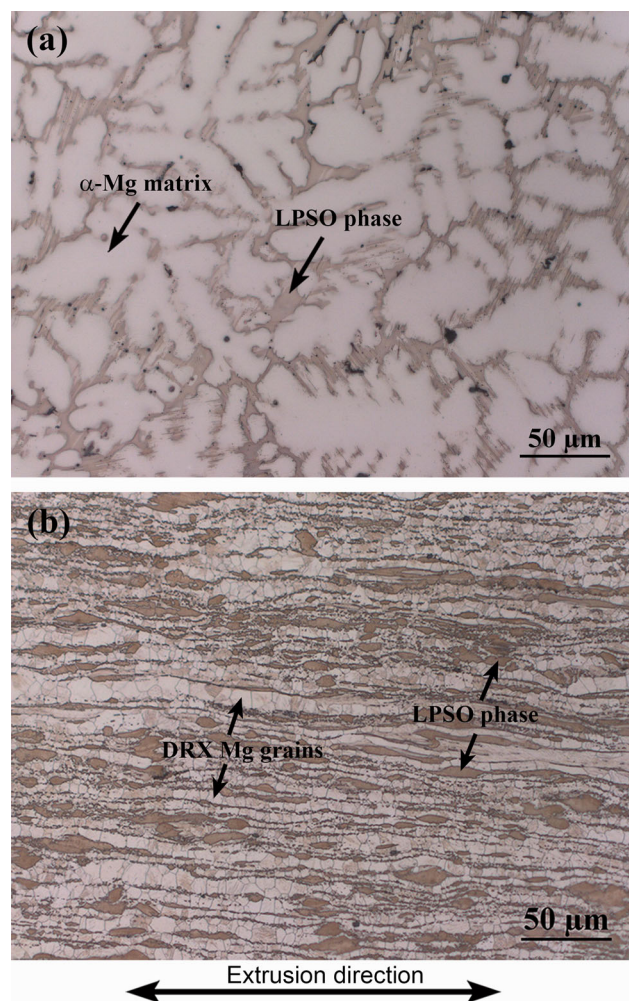

Fig. 2— Optical micrographs of the $Mg_{97}Y_2Zn_1$ alloy in the (*a*) as-cast condition and (*b*) as-extruded condition.

Figures 3(b) and (c). It shows that LPSO existed both as interdendritic fibers and as small plates embedded in Mg grains. Those LPSO plates have the orientation
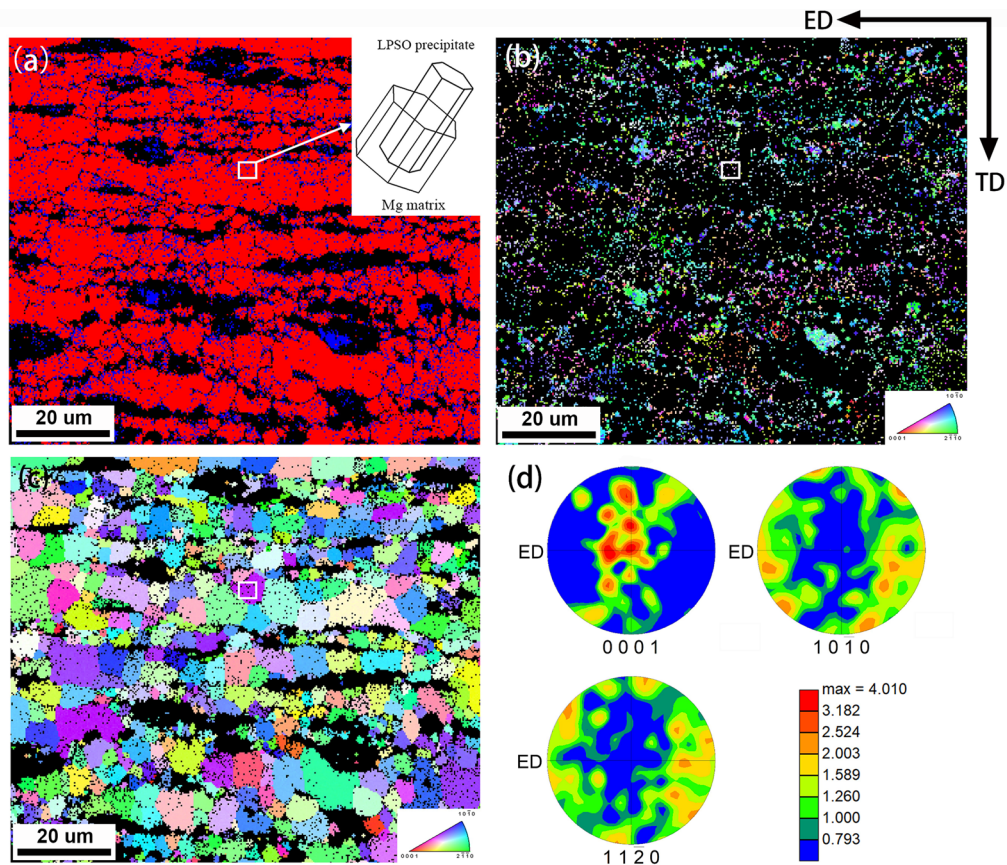
Fig. 3— (a) EBSD phase map of the as-extruded $Mg_{97}Y_2Zn_1$ alloy in which the red color represents Mg phase and the blue color represents LPSO phase. The inset demonstrates that LPSO plates within the Mg phase have the orientation relationship of $\{0001\}_{LPSO}\|\{0001\}_{Mg}$. (b) IPF map of the LPSO phase. (c) IPF map of the Mg phase. (d) $\{0001\}$, $\{10\bar{1}0\}$ and $\{11\bar{2}0\}$ pole figures for the Mg phase for the scanned area.

relationship of $\{0001\}_{LPSO}\|\{0001\}_{Mg}$ with respect to its surrounding Mg grains, as illustrated in the inset in Figure 3(a). Figure 3(d) shows pole figures (PF) for the Mg phase. From the $\{0001\}$ pole figure, although most grains still have their c-axis far away from the extrusion direction (ED), the texture is weaker than most extruded Mg alloys, such as AZ31.[37] It will be shown later that the relatively weak texture plays a critical role for the high ductility of this material.

B. Phase Identification and In Situ Test with Synchrotron X-ray Diffraction

Figure 4(a) shows the synchrotron X-ray diffraction pattern of the tensile specimen prior to deformation. The diffraction pattern is composed of Debye rings, which is typical for polycrystalline materials. In the diffraction pattern, the axial direction (i.e., tensile axis) is parallel to the extrusion direction, while the transverse direction is perpendicular to both the tensile axis and the beam direction (see Figure 1). The 2D diffraction pattern was integrated into conventional diffraction profiles (i.e., intensity vs 2θ) using the software Fit2D (http://www.esrf.eu/computing/scientific/FIT2D/). The integrations were carried out over a ± 5 deg azimuth range around both the axial and the transverse

directions, as practiced in similar studies.[26,32] Figure 4(b) shows the integrated diffraction profiles in both axial and transverse directions. Peaks were fitted to Gaussian functions using the Origin^{TM} software. For a randomly oriented Mg powder material, the Mg $(10\bar{1}1)$ peak should have the highest diffraction intensity according to the diffraction database. Intensity ratios of Mg $(10\bar{1}0)$, Mg (0002), Mg $(10\bar{1}2)$, Mg $(11\bar{2}0)$, Mg $(10\bar{1}3)$ in relative to the strongest Mg $(10\bar{1}1)$ peak should be 0.25, 0.36, 0.15, 0.12, 0.16, respectively.[38] When the specimen has texture, the relative peak intensity will change. In this specimen along the axial direction, Mg $(10\bar{1}1)$ is still the strongest peak, while the intensity ratios of the other five peaks in relative to it are 0.78, 0.27, 0.16, 0.39, 0.42, respectively. Figure 4(c) compares the intensity ratios of these five peaks in relative to Mg $(10\bar{1}1)$ for this specimen along the axial direction and randomly oriented powder. Apparently, intensity of Mg $(10\bar{1}0)$ and Mg $(11\bar{2}0)$ peaks are relatively high along the axial direction, which is expected from the extrusion texture and in agreement with Figure 3(d). In the vicinity of the Mg (0002) and Mg $(10\bar{1}1)$ peaks, there are three small peaks that do not belong to Mg. They are recognized as the $(4\bar{2}\bar{2}5)$, $(4\bar{2}\bar{2}8)$, and $(4\bar{2}\bar{2}.10)$ peaks of the 18R LPSO phase.[26,39] Peaks of the Mg phase and the LPSO phase are both indexed in Figure 4(b).
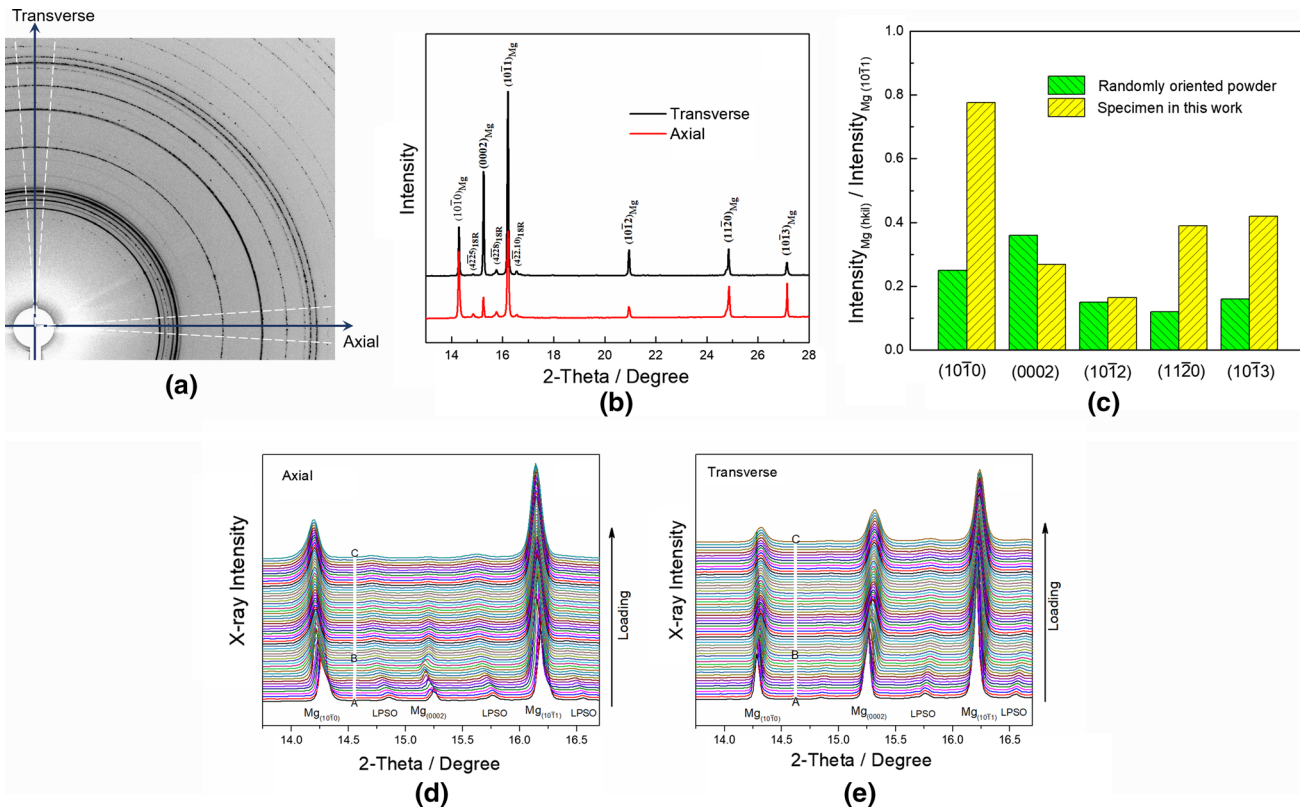
Fig. 4— (*a*) Synchrotron X-ray diffraction pattern of the as-extruded $Mg_{97}Y_2Zn_1$ alloy before the tensile test. The two angular ranges to be integrated are marked by white dotted lines. (*b*) Integrated diffraction profiles along the axial and transverse directions. Peaks of the Mg phase and the LPSO phase are both indexed. (*c*) Intensity ratios of Mg ($10\bar{1}0$), Mg (0002), Mg ($10\bar{1}2$), Mg ($11\bar{2}0$), Mg ($10\bar{1}3$) in relative to the strongest Mg ($10\bar{1}1$) peak for this specimen along the axial direction and for randomly oriented powder. (*d*, *e*) Evolution of diffraction profiles during the tensile test in the axial and the transverse directions.

Figures 4(d) and (e) show the evolution of diffraction profiles during the tensile test. Upon loading, the diffraction peaks in the axial direction shifted towards smaller 2θ values (point A to point B). Because the lattice spacing *d* is inversely related to the Bragg angle, the observed peak shift indicates lattice expansion. In contrast, the diffraction peaks in the transverse direction shifted towards larger 2θ values, indicating lattice contraction. This behavior is expected from the Poisson's effect.[40] As the tensile strain further increased (point B to point C), peak shifting slowed down but peak broadening became significant. The observed peak shifting and peak broadening are caused by the microstructure change during deformation, which will be analyzed in the next sections.

C. *Lattice Strain Analysis*

Figure 5(a) shows the tensile stress–strain curve from the *in situ* test. The specimen showed high strength and good ductility. Its yield strength (YS), ultimate tensile strength (UTS), and elongation to failure are 177 MPa, 285 MPa, and 16.7 pct, respectively. A high strain hardening rate is found.

Figure 5(b) shows the lattice strain values as a function of the applied stress up to the UTS for Mg ($10\bar{1}0$), Mg (0002), Mg ($10\bar{1}1$), Mg ($10\bar{1}2$), Mg ($11\bar{2}0$),

Mg ($10\bar{1}3$), LPSO ($4\bar{2}\bar{2}5$), LPSO ($4\bar{2}\bar{2}8$), and LPSO ($4\bar{2}2.10$) peaks in axial and transverse directions. For each peak, its lattice strain increased in the axial direction (*i.e.*, the loading direction) while decreased in the transverse direction as a result of the Poisson's effect. From the lattice strain development in the elastic stage, elastic moduli along individual (hkl) plane normals can be determined by linear least squares fitting. The result is summarized in Table I. It turns out that the elastic moduli of the LPSO phase are close to the Mg phase. This finding is notably different from the result in Reference 41, which reported the elastic modulus of single crystal 18R LPSO in a $Mg_{85}Y_9Zn_6$ is 65 GPa along $\langle 0001 \rangle$ and 54 GPa along $\langle 11\bar{2}0 \rangle$ based on the measurement using resonant ultrasound spectroscopy and electromagnetic acoustic resonance. The higher concentration of Y and Zn atoms in the latter alloy may cause the higher elastic stiffness.

Upon the start of plastic deformation (*i.e.*, when the applied stress exceeded the yield stress of 177 MPa), lattice strain of certain Mg peaks significantly reduced. In contrast, lattice strain of LPSO peaks increased further. This observation indicates the occurrence of load transfer from the Mg phase to the LPSO phase.[21,24] Figure 6(a) shows lattice strain evolution with the engineering strain for various peaks. The three LPSO peaks developed much higher lattice strain than
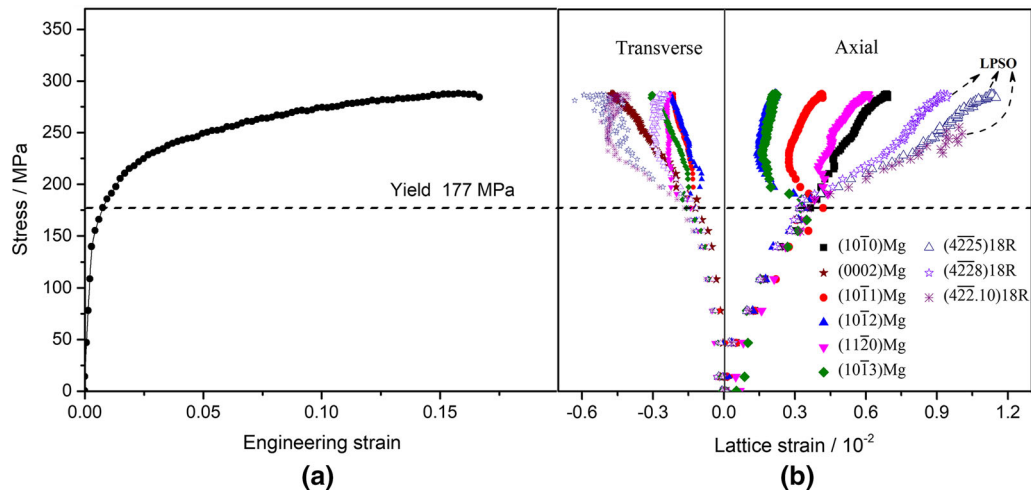
Fig. 5— (*a*) Tensile stress–strain curve of the specimen from the *in situ* test. (*b*) Axial and transverse lattice strains as a function of the applied stress during the *in situ* tensile test.

Table I.   Elastic Moduli (in GPa) and Poisson Ratio (*v*) Along Individual (hkl) Plane Normals in Both Mg and LPSO Phases

Elastic Modulus	Axial	Transverse	Poisson Ratio
($10\bar{1}0$) Mg	51.9	− 172.5	0.30
(0002) Mg	45.6	− 219.3	0.21
($10\bar{1}1$) Mg	44.5	− 119.2	0.37
($10\bar{1}2$) Mg	54.8	− 104.0	0.53
($11\bar{2}0$) Mg	55.9	− 218.5	0.26
($10\bar{1}3$) Mg	56.4	− 179.0	0.32
($4\bar{2}\bar{2}5$) 18R	49.4	− 172.0	0.29
($4\bar{2}\bar{2}8$) 18R	55.7	− 207.6	0.27
($4\bar{2}\bar{2}.10$) 18R	48.5	− 136.3	0.36

the six Mg peaks after 2.0 pct engineering strain, which confirms the load transfer from Mg to LPSO.

Different Mg peaks show different lattice strain behaviors. Lattice strain of Mg ($10\bar{1}2$) sharply decreased after about 0.9 pct engineering strain. As illustrated in Figure 6(b), the Mg ($10\bar{1}2$) peak observed in the axial direction corresponds to those grains with their ($10\bar{1}2$) planes being nearly perpendicular to the tensile axis, which are perfectly oriented for basal slip. Activation of basal slip in these grains and the subsequent stress relief would cause the observed lattice strain decrease of Mg ($10\bar{1}2$). Lattice strain of Mg (0002) increased after 0.9 pct engineering strain, but then decreased after about 2.0 pct engineering strain. The Mg (0002) peak observed in the axial direction corresponds to those grains with their *c*-axis being about 7.6 deg (θ value for Mg (0002), see Figure 4(b)) from the tensile axis. These grains have high Schmid factor (SF) for the activation of {$10\bar{1}2$} deformation twinning (SF = 0.49). The observed lattice strain decrease of Mg (0002) can be attributed to the activation of deformation twinning. Unlike Mg ($10\bar{1}2$) and Mg (0002), lattice strain of Mg ($10\bar{1}0$) did not show apparent decrease during the tensile test. The Mg ($10\bar{1}0$) peak corresponds to those grains with their *c*-axis being approximately perpendicular to the tensile axis, where

both basal slip and deformation twinning are difficult to be activated. The observed lattice strain increase for Mg ($10\bar{1}0$) suggests that those grains had little amount of plastic deformation.

D. *Peak Intensity Analysis*

Plastic deformation is often associated with texture change, which can be analyzed from the change of intensity of different peaks. Figure 7 shows the evolution of relative peak intensities of Mg ($10\bar{1}0$), Mg (0002), Mg ($10\bar{1}1$), Mg ($10\bar{1}2$), and Mg ($10\bar{1}3$) as a function of the engineering strain. For each peak, the relative peak intensity is defined as the ratio between the integrated intensity around the axial direction and the integrated intensity around the transverse direction. The relative intensity of Mg ($10\bar{1}0$) increased from 1.5 at the beginning of the test to 4.0 by the end of the test, whereas the relative intensity of Mg (0002) decreased from 0.2 at the beginning of the test to 0.02 by the end of the test. According to the dislocation slip geometry,[40] when a crystal is deformed by tension, the slip direction and the slip plane of the activated slip system will gradually rotate towards the tensile direction. For those grains deformed by basal slip, their *c*-axis would move away from the axial direction towards the transverse direction, reducing the relative intensity of Mg (0002) while increasing the relative intensity of Mg ($10\bar{1}0$). In addition to basal slip, activation of deformation twinning would cause a similar effect by converting some (0002)-oriented grains to ($10\bar{1}0$)-oriented grains. The relative intensity of Mg ($10\bar{1}1$) mildly increased with strain, while the relative intensity of Mg ($10\bar{1}2$) and Mg ($10\bar{1}3$) mildly decreased with strain. This can be explained by the simple fact that Mg ($10\bar{1}1$) is geometrically closer to Mg ($10\bar{1}0$), while Mg ($10\bar{1}2$) and Mg ($10\bar{1}3$) are geometrically closer to Mg (0002). Combining the peak intensity evolution and the lattice strain evolution, it is proposed that the deformation in the
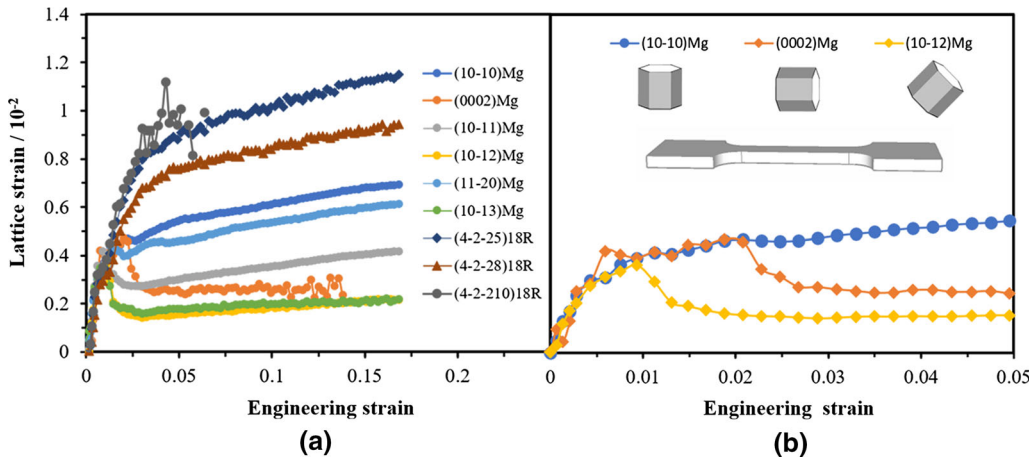
Fig. 6— (a) Lattice strain evolution for Mg and LPSO peaks as a function of the engineering strain in the axial direction. (b) Lattice strain evolution for selected Mg peaks up to 5.0 pct engineering strain.
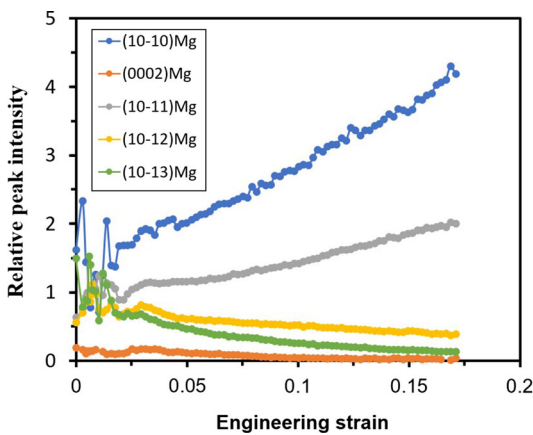

Fig. 7— Evolution of relative peak intensity for selected Mg peaks as a function of the engineering strain.

Mg phase was dominated by basal slip and deformation twinning.

E. EBSD-Based Slip Trace Analysis

To further verify the active deformation mechanisms, EBSD-based slip trace analysis was performed. A rectangular sample was extracted from the extruded material and deformed by a self-made four-point bending apparatus[42] to achieve an equivalent tensile strain of ~1.5 pct and then ~3.0 pct on the top surface (estimated from the curvature of the sample after bending). As shown in Figure 8(a), slip traces developed after deformation. With the grain orientations measured by EBSD (Figure 8(b)), slip trace analysis was performed for the numbered grains in this area. It is found that almost all slip lines correspond to basal slip traces, as marked by red lines in individual grains. Table II shows the highest Schmid factors for basal slip, prismatic slip, pyramidal ⟨c + a⟩ slip, and {1012} twinning for those numbered grains in Figure 8(b) that developed

slip traces or twins. The identified deformation mechanism(s) in each grain are also shown in the table. Apparently, basal slip was the dominant slip type even in those grains with relatively low Schmid factor for basal slip (e.g., Grain 1 and 16). A lenticular deformation twin was observed in Grain 7 at ~1.5 pct strain and grew larger at ~3.0 pct strain. A twin nucleation event was identified in Grain 2 between ~1.5 pct strain and ~3.0 pct strain. The slip trace analysis in Figure 8 confirms that basal slip and deformation twinning are the dominant deformation mechanisms in the Mg phase while prismatic slip and pyramidal ⟨c + a⟩ slip were generally inactive in this alloy.

F. Peak Broadening Analysis

During the tensile test, not only peak position but also peak width (i.e., FWHM) gradually changed with strain. FWHM of different Mg peaks in the transverse direction were plotted as a function of the engineering strain in Figure 9(a). After initial fluctuation, FWHM of all Mg peaks increased rapidly with the engineering strain. Peak broadening is usually composed of strain broadening (e.g., microstrain due to dislocation-like defects) and size broadening (e.g., shrinkage of the coherent scattering volume). Using the Williamson–Hall (W–H) method, it is possible to separate strain broadening and size broadening.[43] According to the theory, size broadening is independent of the diffraction vector length $g_{hkl} = \frac{1}{d_{hkl}}$ of peak (hkl), where d_{hkl} is the d-spacing of the (hkl) plane, while strain broadening proportionally increases with g_{hkl}. A W–H plot shows $FWHM_{hkl}$ vs g_{hkl} for different (hkl) peaks. Figure 10 shows W–H plots at three different strains: 0.9 pct (after yielding), 5.2 pct, and 16.7 pct (last data point before specimen failure). In a W–H plot, the slope of the linear trend-line corresponds to the strain broadening and is proportional to the square root of the mobile dislocation density ($\sqrt{\rho}$); the y-intercept corresponds to the size broadening and is inversely proportional to the coherent scattering domain size D.[43,44] From Figure 10, the
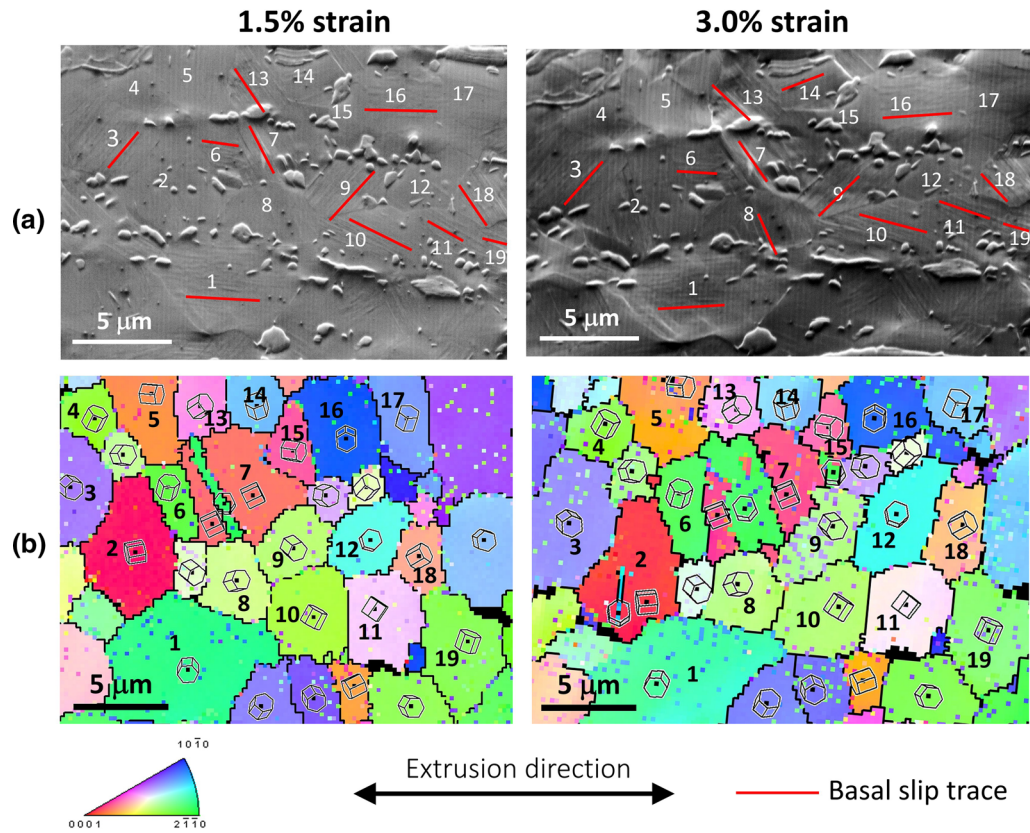
1.5% strain   **3.0% strain**

(a)

(b)

Extrusion direction   —— Basal slip trace

Fig. 8—(*a*) Secondary electron images show slip traces on the surface of a rectangular sample after four-point bending. The equivalent tensile strain was ~1.5 pct and then ~3.0 pct. Slip trace analysis indicates that the observed slip lines correspond to basal slip traces in most grains, as marked by the red lines. (*b*) EBSD IPF maps of the same area as (a) (Color figure online).

Table II. The Maximum Schmid Factors (SF) for Different Deformation Modes in Selected Grains in Fig. 8

Grain	SF_{basal}	$SF_{prismatic}$	$SF_{pyramidal\langle c+a\rangle}$	$SF_{twinning}$	Deformation Mechanism
1	0.04	0.12	0.44	− 0.01	basal slip
2	0.21	0.03	0.48	0.47	twinning
3	0.35	0.40	0.44	0.03	basal slip
6	0.18	0.43	0.46	0.02	basal slip
7	0.28	0.10	0.49	0.40	basal slip + twinning
8	0.28	0.11	0.41	0.13	basal slip
9	0.25	0.09	0.42	0.11	basal slip
10	0.41	0.36	0.41	0.11	basal slip
11	0.43	0.35	0.41	0.12	basal slip
13	0.39	0.20	0.32	0.19	basal slip
14	0.18	0.29	0.49	− 0.03	basal slip
16	0.01	0.47	0.42	− 0.09	basal slip
18	0.48	0.21	0.19	0.28	basal slip
19	0.29	0.42	0.46	0.05	basal slip

strain broadening part (slope of the trend-line) increased rapidly with the engineering strain.

To understand the evolution of dislocation and coherent scattering domain size during deformation, the slopes and y-intercepts obtained from the W–H plots at different strains are calculated and plotted as a function of the engineering strain in Figure 11(a). Figure 11(b) shows the R-square values associated with

the linear fitting for the W–H slope and y-intercept values. The R-square value was relatively small in the very early deformation stage, then it rapidly increased to and maintained around 0.9 till the end of the test. According to Figure 11(b), slopes and y-intercepts obtained from W–H plots are more reliable after plastic deformation started. From Figure 11(a), deformation of the specimen can be divided into two distinct stages. Up
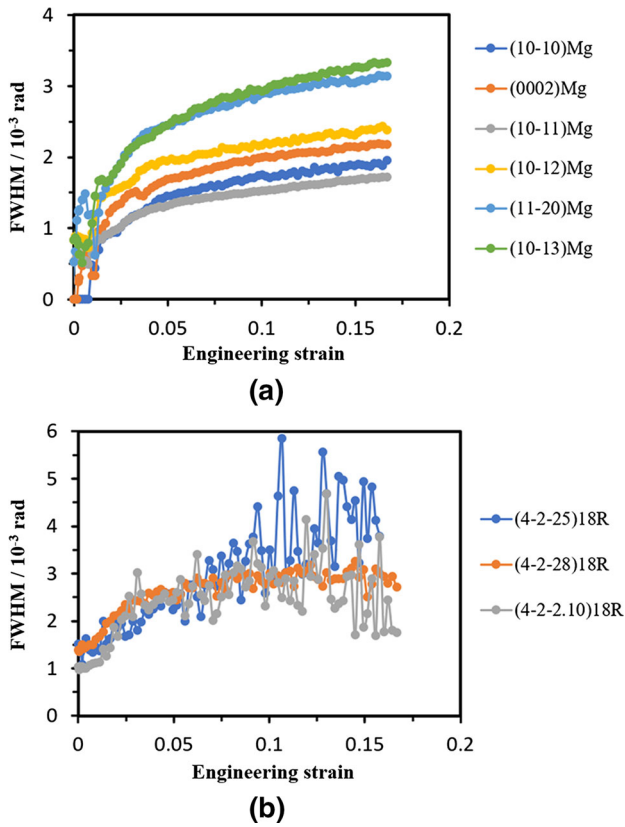
Fig. 9— Evolution of FWHM for (*a*) Mg and (*b*) LPSO peaks along the transverse direction during the tensile test.
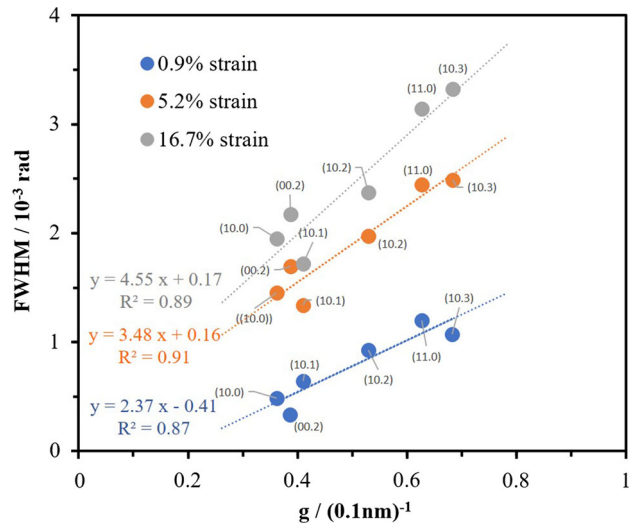

Fig. 10— Williamson–Hall plots for Mg peaks at different strains during the tensile test. A strong dependence of peak width (FWHM) on the diffraction vector length (g) is observed.

to ~4.0 pct strain, the dislocation density in the material (represented by the slope values) increased rapidly. After ~4.0 pct strain, the dislocation density still increased, but at a slower pace. On the other hand, the *y*-intercept value did not change much after 2 pct strain. This observation suggests a continuous increase of the dislocation density in the Mg phase, while the coherent scattering volume remained the same during the plastic deformation regime.

According to the dislocation theory,[40] flow stress in a polycrystal material is linearly related to the square root of the average dislocation density ($\sqrt{\rho}$) as:

$$\sigma = \sigma_0 + M\alpha Gb\sqrt{\rho}, \qquad [2]$$

where G is the shear modulus, b is the length of the Burgers vector, M is the average Taylor factor, and α is a coefficient. Figure 12 shows the change of the W–H slope with the flow stress in the specimen during its deformation. During the plastic deformation regime, the obtained W–H slope almost had a linear relationship with the flow stress value. Hence, the work hardening of this material can be attributed to the increasing dislocation density in the Mg phase.

Compared with Mg, peak width of the LPSO phase only moderately increased (see Figure 9(b)) with strong fluctuation. W–H analysis is not applicable to separate strain broadening and size broadening for the limited number of LPSO peaks.

IV. DISCUSSION

Combining the above results from *in situ* synchrotron XRD and *ex situ* slip trace analysis, we may elucidate the excellent combination of strength and ductility of this Mg-Y-Zn alloy. First of all, it has been found that the LPSO phase developed much higher lattice strain than the Mg matrix after material yielding (Figures 5(b) and 6(a)). Given that the two phases have similar elastic moduli, it means that the LPSO phase behaves like a reinforcing second phase in a metal matrix composite. This reinforcing effect most likely comes from interdendritic LPSO that has a large volume fraction. Secondly, compared with other extruded Mg alloys that exhibit a strong extrusion texture, the Mg-Y-Zn alloy in the present study shows a relatively weak texture (Figure 3), probably due to the presence of interdendritic LPSO phase during hot extrusion.[39] Under such a weak texture, basal slip can be activated in more Mg grains and the material will be more ductile. By contrast, other Mg alloys such as AZ31 with a strong extrusion texture have to resort to non-basal slip modes such as prismatic slip and ⟨c + a⟩ slip to accommodate tensile deformation,[45] which may lead to local stress concentration and ultimate failure of the material.

While some authors suggest that twinning is extremely difficult to be activated in LPSO-containing Mg alloys,[8,12] our finding in Figure 8 shows that twinning can be activated in those Mg grains whose *c*-axis is close to the tensile axis (*e.g.*, Grain 2 and Grain 7 in Figure 8(b)). A recent work by Shao *et al.*[16] found that {10$\bar{1}$2} twins can cross LPSO plates. Since twinning is able to accommodate tensile strain along *c*-axis, nucleation of twins can also enhance the ductility of the material.

Prismatic ⟨a⟩ slip and pyramidal ⟨c + a⟩ slip have been identified in both pure Mg[30,46] due to the strong texture effect and in Mg-Y binary alloys[47,48] due to the solute

(a)
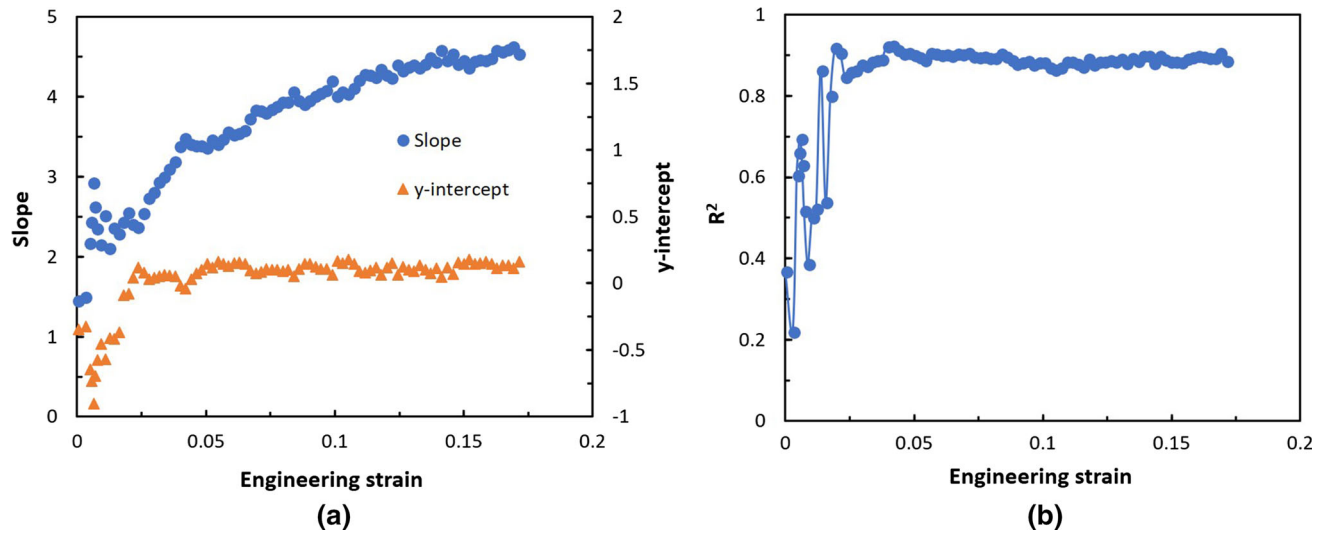

(b)

Fig. 11— (*a*) W–H slope and W–H *y*-intercept values as a function of the engineering strain. (*b*) *R*-square values associated with the linear fitting for the slope and *y*-intercept values.
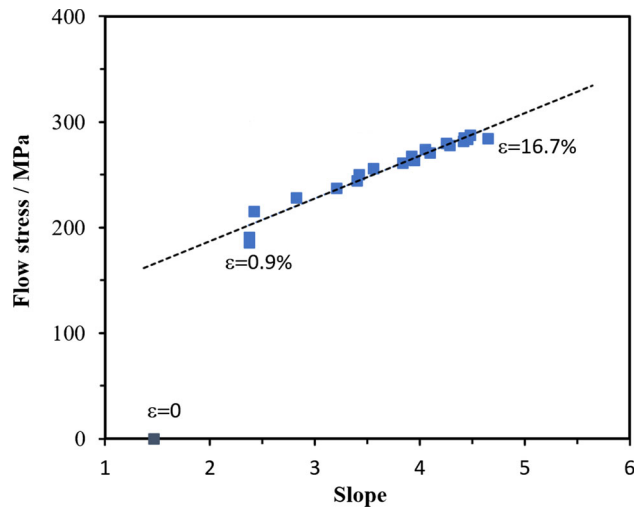

Fig. 12— Correlation between the W–H slope and the instantaneous flow stress in the specimen during the tensile test. The flow stress (applied stress) in the material was linearly related to the W–H slope from 0.9 pct strain to the end of the test.

Y effect. Nevertheless, those non-basal slip modes were found to have minor role in the deformation of this Mg-Y-Zn alloy. This observation may be explained by two reasons. First, the weak texture in this material allows more grains to deform by basal slip and thus reduces the necessity for non-basal slip to be activated. Second, instead of existing in the solid solution state, Y atoms concentrate in the LPSO phase in this Mg-Y-Zn alloy. In such case, CRSS ratio between non-basal slip and basal slip probably remains high in comparison to Mg-Y binary alloys. Nonetheless, we only examined surface slip traces in a sample up to ~3.0 pct strain. It is possible for non-basal slip to have been activated in late deformation when a complicated stress state existed in many grains. For example, Kim *et al.* reported the observation of both basal ⟨a⟩ slip and pyramidal ⟨c + a⟩

slip in a $Mg_{97}Y_2Zn_1$ alloy after cold rolling by 5 pct reduction of thickness.[9]

It was reported that LPSO plates in the Mg phase serve as dislocation nucleation sites because of local lattice mismatch,[9] which may explain the observation in this work that the dislocation density was escalating during the entire tensile test (Figure 11). This is another contributing factor for the good ductility and high work hardening rate in this material. An elasto-plastic self-consistent (EPSC) model (*e.g.*, Reference 49) is being developed to account for the experimental measurement of the stress–strain curve and lattice strain evolution.

V. CONCLUSIONS

Room temperature tensile deformation and microstructure evolution of an extruded $Mg_{97}Y_2Zn_1$ alloy that contains LPSO phase were studied using *in situ* synchrotron X-ray diffraction. The following conclusions are reached:

From lattice strain evolution in the elastic stage, the elastic modulus of the LPSO phase is estimated to be in the 45-55 GPa range, which is similar as Mg. After material yielding, lattice strain in Mg reduced while lattice strain in LPSO increased, indicating the load transfer effect from Mg to LPSO. This observation confirms that LPSO directly strengthens the material like a reinforcing second phase.

Analysis of the lattice strain of different Mg peaks indicates that basal slip was the dominant deformation mechanism. Twinning can also be activated in some grains with favorable orientations. Non-basal slip systems were generally inactive. This finding is confirmed by surface slip trace analysis. The weak extrusion texture due to the presence of interdendritic LPSO allows more grains to be deformed by basal slip, which explains the high ductility of this material.

From peak broadening analysis, dislocation density in the Mg phase was escalating throughout the tensile test. The small LPSO plates within the Mg phase may have served as dislocation nucleation sites. This can explain the high work hardening rate in this material.

REFERENCES

1. B.L. Mordike and T. Ebert: *Mater. Sci. Eng. A*, 2001, vol. 302, pp. 37–45.
2. Y. Kawamura, K. Hayashi, A. Inoue, and T. Masumoto: *Mater. Trans.*, 2001, vol. 42, pp. 1172–76.
3. A. Inoue, Y. Kawamura, M. Matsushita, K. Hayashi, and J. Koike: *J. Mater. Res.*, 2001, vol. 16, pp. 1894–1900.
4. D. Egusa and E. Abe: *Acta Mater.*, 2012, vol. 60, pp. 166–78.
5. Y.M. Zhu, A.J. Morton, and J.F. Nie: *Acta Mater.*, 2010, vol. 58, pp. 2936–47.
6. E. Abe, Y. Kawamura, K. Hayashi, and A. Inoue: *Acta Mater.*, 2002, vol. 50, pp. 3845–57.
7. X.H. Shao, Z.Q. Yang, and X.L. Ma: *Acta Mater.*, 2010, vol. 58, pp. 4760–71.
8. K. Hagihara, N. Yokotani, and Y. Umakoshi: *Intermetallics*, 2010, vol. 18, pp. 267–76.
9. J.K. Kim, S. Sandlöbes, and D. Raabe: *Acta Mater.*, 2015, vol. 82, pp. 414–23.
10. R. Chen, S. Sandlöbes, X.Q. Zeng, D.J. Li, S. Korte-Kerzel, and D. Raabe: *Mater. Sci. Eng. A*, 2017, vol. 682, pp. 354–58.
11. K. Hagihara, A. Kinoshita, Y. Sugino, M. Yamasaki, Y. Kawamura, H.Y. Yasuda, and Y. Umakoshi: *Acta Mater.*, 2010, vol. 58, pp. 6282–93.
12. M. Yamasaki, K. Hagihara, S.I. Inoue, J.P. Hadorn, and Y. Kawamura: *Acta Mater.*, 2013, vol. 61, pp. 2065–76.
13. M. Yamasaki, K. Hashimoto, K. Hagihara, and Y. Kawamura: *Acta Mater.*, 2011, vol. 59, pp. 3646–58.
14. K. Hagihara, M. Yamasaki, M. Honnami, H. Izuno, M. Tane, T. Nakano, and Y. Kawamura: *Philos. Mag.*, 2015, vol. 95, pp. 132–57.
15. M. Okayasu, S. Takeuchi, M. Matsushita, N. Tada, M. Yamasaki, and Y. Kawamura: *Mater. Sci. Eng. A*, 2016, vol. 652, pp. 14–29.
16. X.H. Shao, Z.Z. Peng, Q.Q. Jin, and X.L. Ma: *Acta Mater.*, 2016, vol. 118, pp. 177–86.
17. H. Liu, J. Bai, K. Yan, J.L. Yan, A.B. Ma, and J.H. Jiang: *Mater. Des.*, 2016, vol. 93, pp. 9–18.
18. W. Liu, J.S. Zhang, C.X. Xu, X.M. Zong, J.Q. Hao, Y. Li, and Z. Zhang: *Mater. Des.*, 2016, vol. 110, pp. 1–9.
19. P. Willmott: *An Introduction to Synchrotron Radiation: Techniques and Applications*, Wiley, New York, 2011.
20. L.Y. Wang, M.M. Li, J. Almer, T. Bieler, and R. Barabash: *Front. Mater. Sci.*, 2013, vol. 7, pp. 156–69.
21. M.L. Young, J.D. Almer, M.R. Daymond, D.R. Haeffner, and D.C. Dunand: *Acta Mater.*, 2007, vol. 55, pp. 1999–2011.
22. M.A. Weisser, A.D. Evans, S.V. Petegem, S.R. Holdsworth, and H.V. Swygenhoven: *Acta Mater.*, 2011, vol. 59, pp. 4448–57.
23. L.Y. Wang, M.M. Li, and J. Almer: *J. Nucl. Mater.*, 2013, vol. 440, pp. 81–90.
24. S.R. Kada, P.A. Lynch, J.A. Kimpton, and M.R. Barnett: *Acta Mater.*, 2016, vol. 119, pp. 145–56.
25. Y.B. Miao, K. Mo, Z.J. Zhou, X. Liu, K. Lan, G.M. Zhang, J. Park, J. Almer, and J.F. Stubbins: *Mater. Des.*, 2016, vol. 111, pp. 622–30.
26. G. Garces, D.G. Morris, M.A. Muñoz-Morris, P. Perez, D. Tolnai, C. Mendis, A. Stark, H.K. Lim, S. Kim, N. Shell, and P. Adeva: *Acta Mater.*, 2015, vol. 94, pp. 78–86.
27. S.B. Yi, C.H.J. Davies, H.G. Brokmeier, R.E. Bolmaro, K.U. Kainer, and J. Homeyer: *Acta Mater.*, 2006, vol. 54, pp. 549–62.
28. M. Lentz, M. Klaus, I.J. Beyerlein, M. Zecevic, W. Reimers, and M. Knezevic: *Acta Mater.*, 2015, vol. 86, pp. 254–68.
29. L. Lu, J.W. Huang, D. Fan, B.X. Bie, T. Sun, K. Fezzaa, X.L. Gong, and S.N. Luo: *Acta Mater.*, 2016, vol. 120, pp. 86–94.
30. K. Máthis, K. Nyilas, A. Axt, I. Dragomir-Cernatescu, T. Ungár, and P. Lukáč: *Acta Mater.*, 2004, vol. 52, pp. 2889–94.
31. T. Ungár, A.D. Stoica, G. Tichy, and X.L. Wang: *Acta Mater.*, 2014, vol. 66, pp. 251–61.
32. L.Y. Wang, M.M. Li, and J. Almer: *Acta Mater.*, 2014, vol. 62, pp. 239–49.
33. M.M. Li, L.Y. Wang, and J.D. Almer: *Acta Mater.*, 2014, vol. 76, pp. 381–93.
34. T.R. Bieler, M.A. Crimp, Y. Yang, L. Wang, P. Eisenlohr, D.E. Mason, W. Liu, and G.E. Ice: *JOM*, 2009, vol. 61, pp. 45–52.
35. T.Y. Yang, W. Wen, G.Z. Yin, X.L. Li, M. Gao, Y.L. Gu, L. Li, Y. Liu, H. Lin, X.M. Zhang, B. Zhao, T.K. Liu, Y.G. Yang, Z. Li, X.T. Zhou, and X.Y. Gao: *Nucl. Sci. Tech.*, 2015, vol. 26, pp. 1–5.
36. H. Okuda, T. Horiuchi, S. Hifumi, M. Yamasaki, Y. Kawamura, and S. Kimura: *Metall. Mater. Trans. A*, 2014, vol. 45, pp. 4780–85.
37. H. Yu, C. Li, Y. Xin, A. Chapuis, X. Huang, and Q. Liu: *Acta Mater.*, 2017, vol. 128, pp. 313–26.
38. Natl. Bur. Stand. (U. S.) Monogr. 25, 1985, Section 21, pp. 82.
39. G. Garces, P. Perez, S. Cabeza, S. Kabra, W. Gan, and P. Adeva: *Metall. Mater. Trans. A*, 2017, vol. 48, pp. 5332–43.
40. M.A. Meyers K.K. Chawla : *Mechanical Behavior of Materials* , 2nd ed. , Cambridge University Press, Cambridge, 2016 , pp. 381 88 .
41. M. Tane, Y. Nagai, H. Kimizuka, K. Hagihara, and Y. Kawamura: *Acta Mater.*, 2013, vol. 61, pp. 6338–51.
42. L. Wang, Y. Yang, P. Eisenlohr, T.R. Bieler, M.A. Crimp, and D.E. Mason: *Metall. Mater. Trans. A*, 2010, vol. 41, pp. 421–30.
43. G.K. Williamson and W.H. Hall: *Acta Metall.*, 1953, vol. 1, pp. 22–31.
44. T. Ungar and G. Tichy: *Phys. Stat. Sol. A*, 1999, vol. 171, pp. 425–34.
45. Y. Wang and H. Choo: *Acta Mater.*, 2014, vol. 81, pp. 83–97.
46. C.M. Cepeda-Jiménez, J.M. Molina-Aldareguia, and M.T. Pérez-Prado: *Acta Mater.*, 2015, vol. 84, pp. 443–56.
47. S. Sandlöbes, S. Zaefferer, I. Schestakow, S. Yi, and R. Gonzalez-Martinez: *Acta Mater.*, 2011, vol. 59, pp. 429–39.
48. Z. Huang, L. Wang, B. Zhou, T. Fischer, S. Yi, and X. Zeng: *Scripta Mater.*, 2018, vol. 143, pp. 44–48.
49. J.J. Bhattacharyya, F. Wang, N. Stanford, and S.R. Agnew: *Acta Mater.*, 2018, vol. 146, pp. 55–62.